



# Study on the mechanical and damage properties of laminated limestone under acid mine drainage dissolution

Chengyuan Ding · Shuangying Zuo ·  
Yunchuan Mo

Received: 3 August 2023 / Accepted: 19 May 2024  
© The Author(s) 2024

**Abstract** To explore the chemical and mechanical effects of acid mine drainage on water and rock, acid mine drainage (AMD) dissolution tests, triaxial compression tests, and acoustic emission tests were performed on limestone rock samples with different bedding dip angles. Combined with scanning electron microscopy and nuclear magnetic resonance analyses, the changes in the internal pores and surface morphologies of the rock samples before and after dissolution were analyzed. The results were as follows. (1) AMD dissolution mainly occurred in the shallow surfaces and bedding planes of the limestone samples. During dissolution, the shape of the matrix crystal disappeared to form small pores, and residual substances appeared during the dissolution of the bedding plane. These small pores were prone to the creation of large honeycomb-like dissolved pores. (2) With increasing bedding plane angle, the compressive

strengths and elastic moduli of the limestone samples exhibited V-shaped distributions. Additional branch cracks were derived from the limestone samples after dissolution, and dissolution reduced the mechanical strength of the limestone by decreasing the crack initiation stress and damage stress. (3) With increasing bedding dip angle, the uniaxial failure modes of the rock samples changed from matrix tensile failure and shear failure along the bedding plane to plane tensile failure. After dissolution, the limestone matrix was prone to cracking and spalling along the surface of the sample. (4) There were differences in the triaxial compression failure modes between the dissolved limestone and the undissolved limestone. When  $\alpha=0^\circ$  or  $90^\circ$ , the limestone samples formed additional branch fissures after dissolution. When  $\alpha=45^\circ$ , the formation of penetrating cracks along the bedding plane was obviously controlled by the bedding plane. (5) A chemical–mechanical damage model was established and modified by the compression coefficient  $K$ , which could effectively reflect the deformation of the dissolved rock sample during loading.

---

C. Ding · S. Zuo (✉) · Y. Mo  
College of Resource and Environmental Engineering,  
Guizhou University, Guiyang 550025, Guizhou, China  
e-mail: syzuo@gzu.edu.cn

C. Ding  
e-mail: 1623217533@qq.com

Y. Mo  
e-mail: 1813784471@qq.com

S. Zuo  
Key Laboratory of Karst Geological Resources  
and Environment, Ministry of Education, Guizhou  
University, Guiyang 550025, Guizhou, China

## Article highlights

- The difference between the limestone matrix and bedding surface under the dissolution of AMD was investigated.
- Relationships among the mechanical properties, bedding dip angles, and damage evolution char-

acteristics of specimens subjected to AMD were revealed.

- A chemical–mechanical damage model modified by the compression coefficient  $K$  was established.

**Keywords** AMD · Laminated rock · Soaking corrosion in an acidic environment · Mechanical properties · Chemical–mechanical damage model

## 1 Introduction

The development and utilization of coal mine resources have greatly contributed to human industrial production and daily life. However, more than 3500 coal mines in China have closed in the past 30 years due to the coal resource depletion, resource integration, and clean energy development, among other reasons (Jiang et al. 2020; Zhu et al. 2022). The number of coal mines to be closed will reach 15,000 by 2030, according to statistics from the Chinese Academy of Engineering (Yuan et al. 2018). After closure, drainage stops, and the water level in the mining area rises rapidly, resulting in the output of acid mine drainage (AMD) wastewater characterized by a low pH, high zinc concentration, high sulfate content (Fortes et al. 2022; Retka et al. 2020; Rodríguez et al. 2018; Santos Jallath et al. 2018), heavy pollution and strong corrosiveness (Xia et al. 2023). Under the action of acidic dissolution, the physical and mechanical properties of a rock mass can change (Huang et al. 2021; Xu et al. 2022a, b), impacting the chemical dissolution and stress field imbalance characteristics of carbonate rock overlying the mining site.

To date, some achievements have been made in the study of the dissolution and microstructural characteristics of carbonate rocks under the dissolution of various chemical solutions. The dissolution and karst features of carbonate rocks are closely related to their geological structures, hydrogeological conditions, and lithologies. Chemical composition, mineral composition, pore structure, and particle characteristics have certain influences on dissolution (Bai et al. 2019). The dissolution rate of carbonate is positively proportional to the calcite content, while it decreases with increasing dolomite content (Bai et al. 2019). Limestone rock is more susceptible to acid dissolution than lime dolomite rock under the same acidification

conditions (Zhang et al. 2020). In addition, the micro-section of the rock affects the dissolution of the acid. The rock microstructure can control the acid–rock reaction of dolomite. The looser the microstructure is, the faster the reaction (Xu et al. 2022a, b). During the dissolution of limestone samples in different pH solutions, the porosities undergo different changes. The lower the pH of the solution is, the faster the rate of change in the porosity and the greater the porosity resulting from the intense chemical reaction (Li et al. 2018a; b; Zhang et al. 2022). The pore scales gradually change from the nanoscale to the microscale with decreasing pH; the single pore area and perimeter increase and the fractal dimension decreases (Liu et al. 2023a; b). In an acidic environment, the microscopic pore structure of limestone exhibits fractal characteristics. The fractal dimension first increases, then decreases, and finally increases with increasing soaking time (Chen et al. 2022).

With the continuous occurrence of dissolution, the internal structures, mineral particles, and pores of the rock masses change, in addition to their strengths and parameters. During the dissolution of limestone, chemical corrosion critically influences the propagation of microcracks and accelerates the damage development of the sample (Li et al. 2018a; b); Li et al. reported that the chemical corrosion rate significantly affects the development of microcracks in rocks (Li et al. 2020). In addition, the change in the pH of the chemical solution still affects the mechanical properties of the rock. For example, Liu et al. reported that the mechanical properties (uniaxial compressive strength, elastic modulus, tensile strength, and brittleness index) of a sample decrease with decreasing pH (Liu et al. 2023a; b). Li et al. reported that a change in pH reduces the mechanical properties of rocks by affecting the changes in the porosity and microdamage characteristics (Li et al. 2018a; b). Yang Yu et al. reported a decrease in pH, an increase in dissolution time, an increase in cracking and a decrease in peak strength (Yu et al. 2023). Consequently, limestone exhibits an obvious creep effect in acidic solution, and the lower the pH is, the greater the creep deformation (Jiang et al. 2012). Dissolution affects the failure mode of the sample. Huayan et al. reported that the deformation and failure modes of limestone samples subjected to triaxial compression tests after soaking in chemical solution change from brittle to tough (Huayan et al. 2016).

The above studies were focused on the microstructural, mechanical, and damage evolution properties of rocks undergoing chemical corrosion. Most of these scholars used custom acid solutions to carry out experiments. However, engineering rock masses are mostly present in acid mine drainage environments. The mechanical properties of bedding limestone are significantly affected by dissolution, bedding plane, and time characteristics, among other factors. In this paper, based on AMD samples removed from a closed mine, dissolution tests of limestone samples with different bedding dip angles were performed. Combined with scanning electron microscopy, nuclear magnetic resonance, and other microscopic tests, the changes in the internal pores and surface morphologies of the rock samples before and after dissolution were analyzed. Triaxial compression and acoustic emission tests were conducted on corroded rock samples, and a chemical–mechanical damage model of bedding limestone under AMD dissolution conditions was constructed, providing a theoretical basis for the study of rock mass engineering stability properties in shutting coal mines.

## 2 Sample preparation and test scheme

### 2.1 Sample preparation

The AMD sample was extracted from an abandoned coal mine in Guizhou (Fig. 1). The calcium ion ( $\text{Ca}^{2+}$ ), magnesium ion ( $\text{Mg}^{2+}$ ), total iron concentration, and pH were tested with an atomic absorption



**Fig. 1** Acid mine drainage sampling

**Table 1** Basic parameters of the AMD solution

Basic indicator	$\text{Ca}^{2+}/(\text{mg/L})$	$\text{Mg}^{2+}/(\text{mg/L})$	Total iron/ (mg/L)	pH
Content	20.01	16.54	118	2.54

spectrophotometer and a pHS-3C digital platform pH meter. The basic indicators of the solution are shown in Table 1.

The rock sample was a medium-thick limestone with bedding in the first member of the Lower Triassic Daye Formation ( $T_1d_1$ ). According to the standard test method for engineering rock masses (GB/T 0266-2013), standard cylindrical limestone samples with bedding dip angles of  $0^\circ$ ,  $30^\circ$ ,  $45^\circ$ ,  $60^\circ$  and  $90^\circ$  were prepared (Fig. 2).

### 2.2 Test scheme

#### 1) Dissolution scheme

Each specimen had a different bedding dip angle ( $\alpha=0^\circ$ ,  $30^\circ$ ,  $45^\circ$ ,  $60^\circ$ , and  $90^\circ$ ) and was individually placed in a container and soaked with 1.8 L of AMD solution. Both ends of the rock samples were smeared with preservatives to avoid affecting the subsequent mechanical test results. The initial pH of the acid solution was 2.54, and the total dissolution time was 240 h.

#### 2) Axial and triaxial compression test

To determine the relationships between the mechanical parameters and dissolution damage characteristics, a series of triaxial compression tests were carried out on undissolved and dissolved specimens with different bedding dip angles. The stress–strain curves and acoustic emission (AE) characteristic curves were recorded until the samples were fully destroyed as shown in Table 2.

#### 3) Nuclear magnetic resonance test

Nuclear magnetic resonance (NMR) tests were carried out to determine the fracture locations and propagation modes for the above samples under three

**Fig. 2** Typical limestone samples with different bedding angles

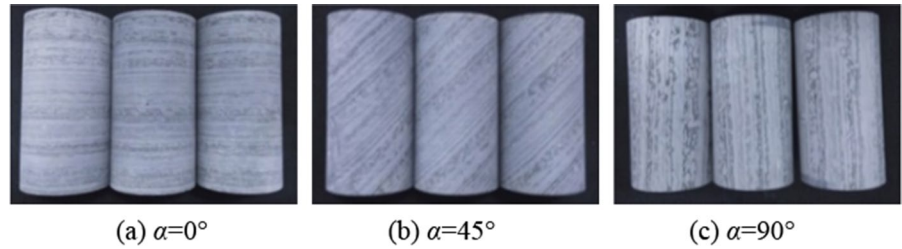


**Table 2** Triaxial compression test scheme for the limestone rock samples

Test condition	Inclination angle of bedding plane/ $^{\circ}$	Confining pressure $\sigma_3$ /MPa	Number of samples
undissolved	0 $^{\circ}$ , 30 $^{\circ}$ , 45 $^{\circ}$ , 60 $^{\circ}$ , 90 $^{\circ}$	0, 5, 10	25
dissolved	0 $^{\circ}$ , 30 $^{\circ}$ , 45 $^{\circ}$ , 60 $^{\circ}$ , 90 $^{\circ}$	0, 5, 10	23*

\*Some problems arose when the samples with bedding angles of 30 $^{\circ}$  were soaked and dissolved; thus, triaxial compression tests with confining pressures of 5 MPa and 10 MPa were not performed.

conditions: before dissolution, after dissolution, and after triaxial compression failure. The MesoMR12-060H-I nuclear magnetic resonance imaging analyzer and the axial section imaging diagram of the limestone samples are shown in Fig. 3.

4) Scanning electron microscopy and energy spectrum tests

Smooth sections of the stroma and bedding plane were selected for scanning electron microscopy

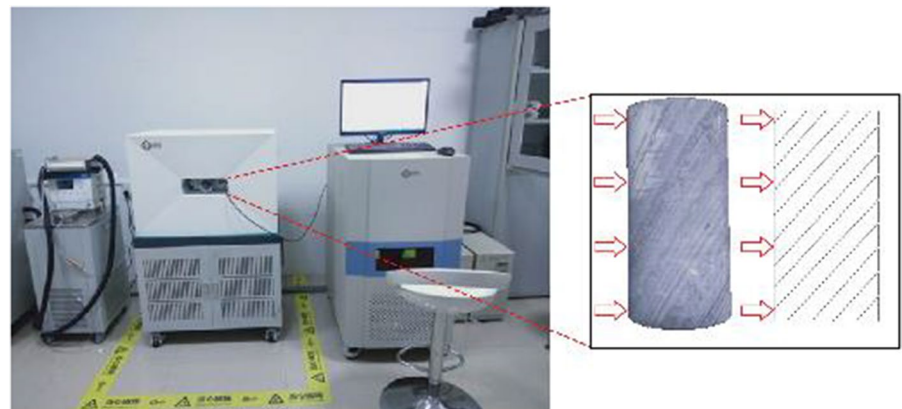
(SEM) and energy spectrum analyses. The experimental design involved observations of the rock specimens at magnifications of 500 $\times$ , 1000 $\times$ , and 2000 $\times$ .

**3 Analysis of the test results**

3.1 Dissolution test

As shown in Fig. 4, as the dissolution time increased, the solution gradually became increasingly turbid as the bedding dip angle increased from  $\alpha = 0^{\circ}$ . The yellow precipitates were attached to the rock surface, and bubbles were observed during dissolution. When the dissolution time reached approximately 48 h, the soaking solution was the most turbid. Then, the solution gradually clarified to a certain extent. After the test was performed, a considerable amount of material precipitated at the bottom of the container, and yellow attachments with bubble structures on the surfaces of the limestone samples were apparent. A layer of white inclusions formed between the yellow precipitate and the rock matrix.

**Fig. 3** MesoMR12-060H-I NMR equipment and sample imaging section



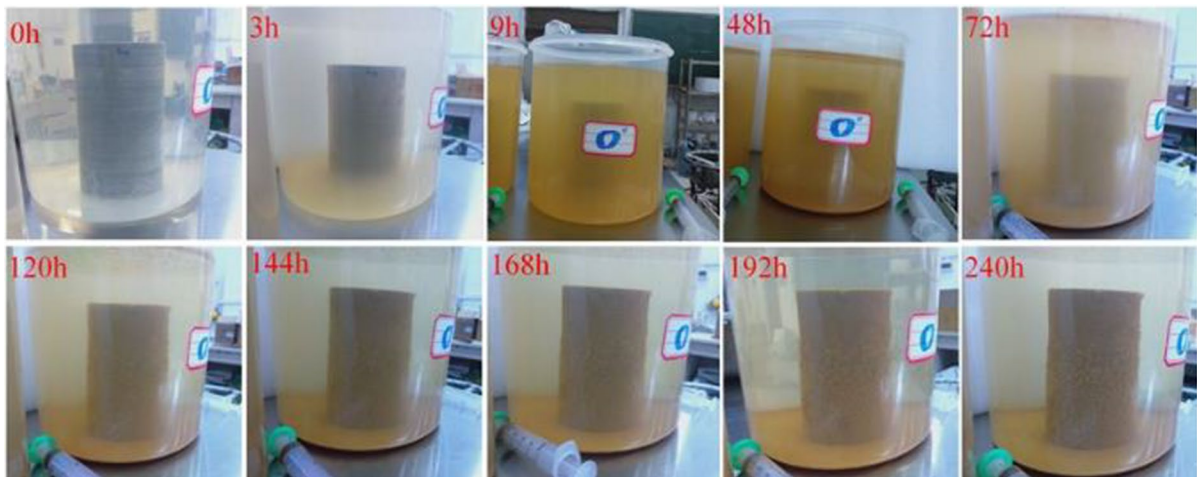


**Fig. 4** Dissolution phenomena at different times ( $\alpha=0^\circ$ )

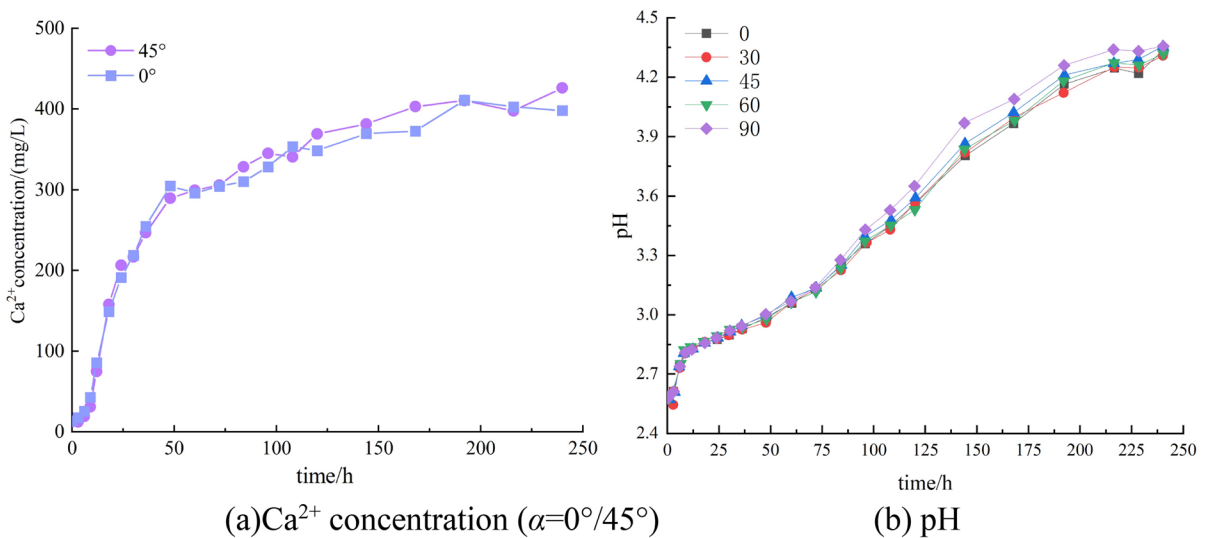


**Fig. 5** Ion concentration in solution at different times

The change in the dissolution process was considered to occur due to the chemical reaction in solution. Figure 5a shows that the concentration of calcium ions ( $Ca^{2+}$ ) in the solution first increased slowly at the beginning of the experiment and then increased rapidly. These changes occurred because the reaction between the AMD and the limestone sample gradually intensified from the surface to the shallow layer of the sample. Moreover, the chemical reaction was enhanced, and the solution gradually

became turbid. When  $t > 50$  h, the growth rate of the  $Ca^{2+}$  concentration was slower than that in the early stage because the precipitated substances attached to the surfaces of the samples hindered the combination of mineral components and reduced the occurrence of chemical reactions. Therefore, during dissolution, the dissolution was weakened after  $t > 48$  h, and the solution gradually clarified.

The bedding effect caused the solute  $Ca^{2+}$  concentration of the limestone rock with  $\alpha=45^\circ$  to be

generally greater than that with  $\alpha=0^\circ$  because the dissolution reaction gradually developed and infiltrated the rock sample from the bedding plane under long-term dissolution conditions. The variations in the  $H^+$  concentrations of the dissolved limestone samples with different dip angles were in the order of  $90^\circ < 45^\circ < 60^\circ < 30^\circ < 0^\circ$ . When  $t > 175$  h, the concentration of  $H^+$  in the solution decreased, and the reactions between  $H^+$  and the mineral components in the limestone decreased in intensity; thus, the  $Ca^{2+}$  concentration tended to stabilize as shown in Fig. 6.

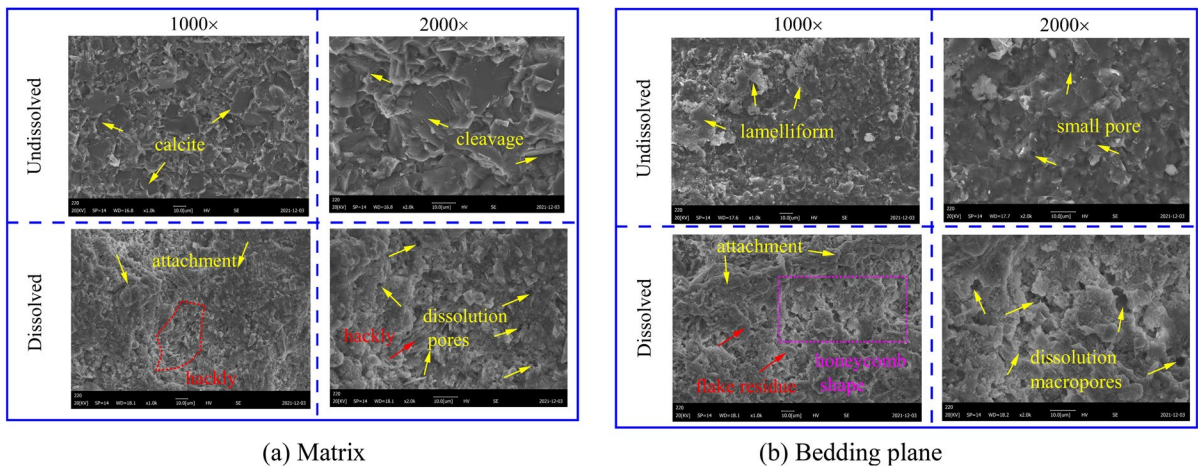
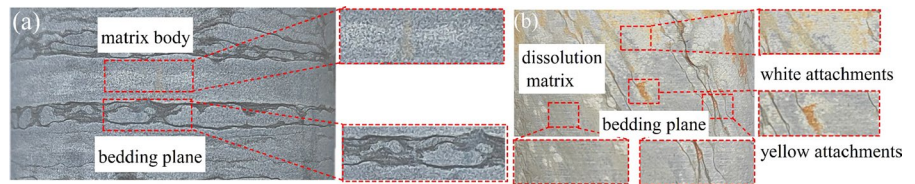
### 3.2 SEM test comparison

As shown in Fig. 7, the bedding planes of the undissolved limestone were primarily considered laminated structures with small pores. The crystals of the fresh limestone matrix were intact and closely related to each other. Tiny holes were present between the local grains with obvious cleavages and clear crystal outlines. After AMD dissolution, the bedding limestone exhibited obvious differential dissolution. The shape of the matrix crystal

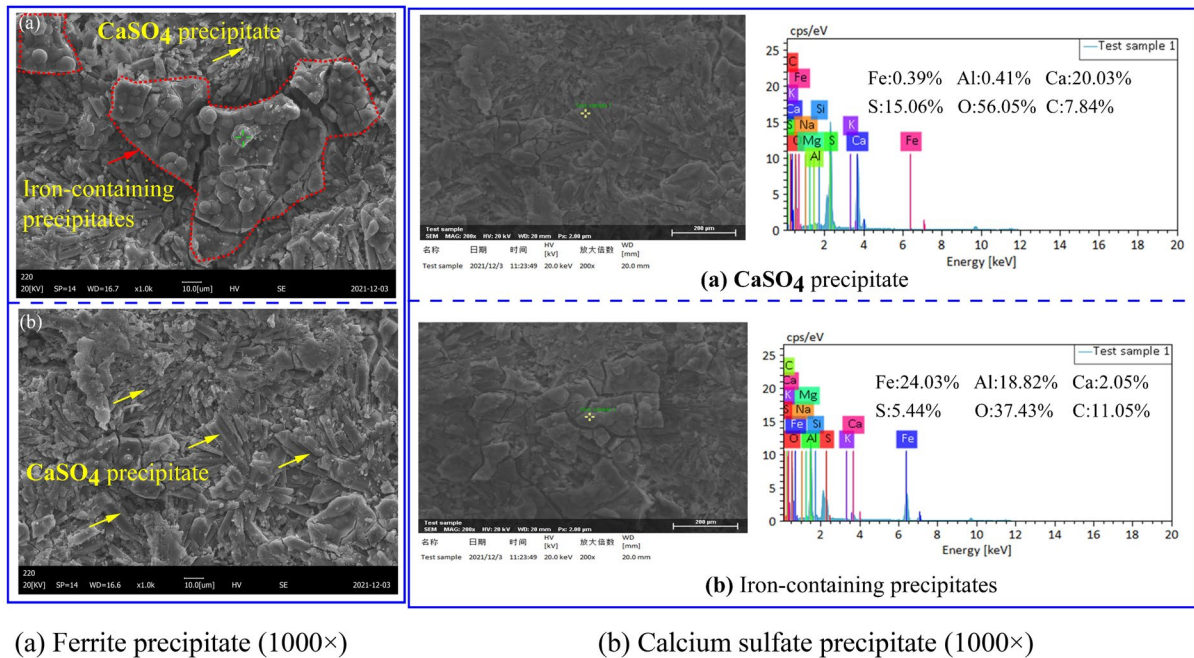
disappeared, and a serrated corrosion morphology formed along the cleavage direction of calcite. Residual substances appeared during the dissolution of the bedding plane, forming honeycomb-like dissolution pores. The corrosion precipitates were attached to the matrix body and the bedding surface. The matrix dissolution easily produced small dissolution pores, and the bedding surface had large dissolution pores. Combined with the analysis of the energy spectrum test results, the limestone matrix was considered to be mainly composed of calcite, which could react with hydrogen ions ( $H^+$ ) to form free calcium ions. The bedding planes contained clay, quartz, feldspar, and other minerals. Moreover, soluble substances were dissolved, and residual substances formed dissolution pores.

Figure 8 shows that the surface attachments of the limestones were mainly calcium sulfate ( $CaSO_4$ ) and iron-containing precipitates. The AMD solution was usually rich in iron ions ( $Fe^{3+}$ ) and sulfate ions ( $SO_4^{2-}$ ), leading to the presence of these attachments. As the limestone reacted with hydrogen ions ( $H^+$ ) in the solution, the concentration of calcium

**Fig. 6** Schematic diagram of the sampling position of SEM: **a** undissolved limestone and **b** dissolved limestone



**Fig. 7** Microstructural characteristics of the bedding planes and matrices of the undissolved limestone samples



**Fig. 8** Characteristics of the dissolution precipitates

ions ( $\text{Ca}^{2+}$ ) increased, and the sulfate ions ( $\text{SO}_4^{2-}$ ) in the solution combined with calcium ions ( $\text{Ca}^{2+}$ ) to form calcium sulfate ( $\text{CaSO}_4$ ) crystals that could be attached to the limestone surface.

### 3.3 Analysis of the mechanical properties of the dissolved limestone samples

#### 3.3.1 Results of the uniaxial compression test

Figure 9 shows the stress–strain curves and AE characteristics of the undissolved and dissolved limestone samples with different bedding angles under uniaxial compression tests. In the compaction stage, the microcracks in the limestone samples were compressed, the stress–strain curves were nonlinear and slightly sunken, and a few AE signals appeared along the direction of crack compaction. Subsequently, the curve entered the linear elastic deformation stage, and no AE signals could be clearly observed. Then, the increasing stress led to the formation of new microcracks, and the mechanical properties of the limestone samples continuously deteriorated. The stress–strain curve deviated from a straight line during the plastic stage, and the

AE signals steadily increased, indicating that additional microcracks constantly occurred inside the samples. Finally, when the stress reached  $\sigma_p$ , a macrofracture plane formed. At this time, the AE signals increased sharply.

The AE signals of the limestone samples were increasingly active after the elastic deformation stage under AMD dissolution conditions, further indicating that dissolution tended to cause chemical damage. The influence of the bedding inclination angle on the AE signal decreased in the order of  $0^\circ > 90^\circ > 60^\circ$  (Fig. 11), which was mainly related to the failure mode. The  $0^\circ$ ,  $90^\circ$ , and  $60^\circ$  rock samples exhibited matrix tensile failure, bedding plane tensile fracture, and shear failure along the plane, respectively, while the AE signals gradually weakened.

According to the uniaxial compression test, the relationships among the uniaxial compressive strengths, the elastic moduli, and the bedding dip angles of the undissolved and dissolved limestone samples are shown in Fig. 10. With increasing angle, the compressive strength and elastic modulus of the limestone samples exhibited V-shaped distributions. Among the five angles, the uniaxial compressive strengths and elastic moduli were

**Fig. 9** Stress–strain–acoustic emission characteristics of limestone rock samples with partial bedding dip angles (uniaxial compression;  $\sigma_3=0$  MPa)

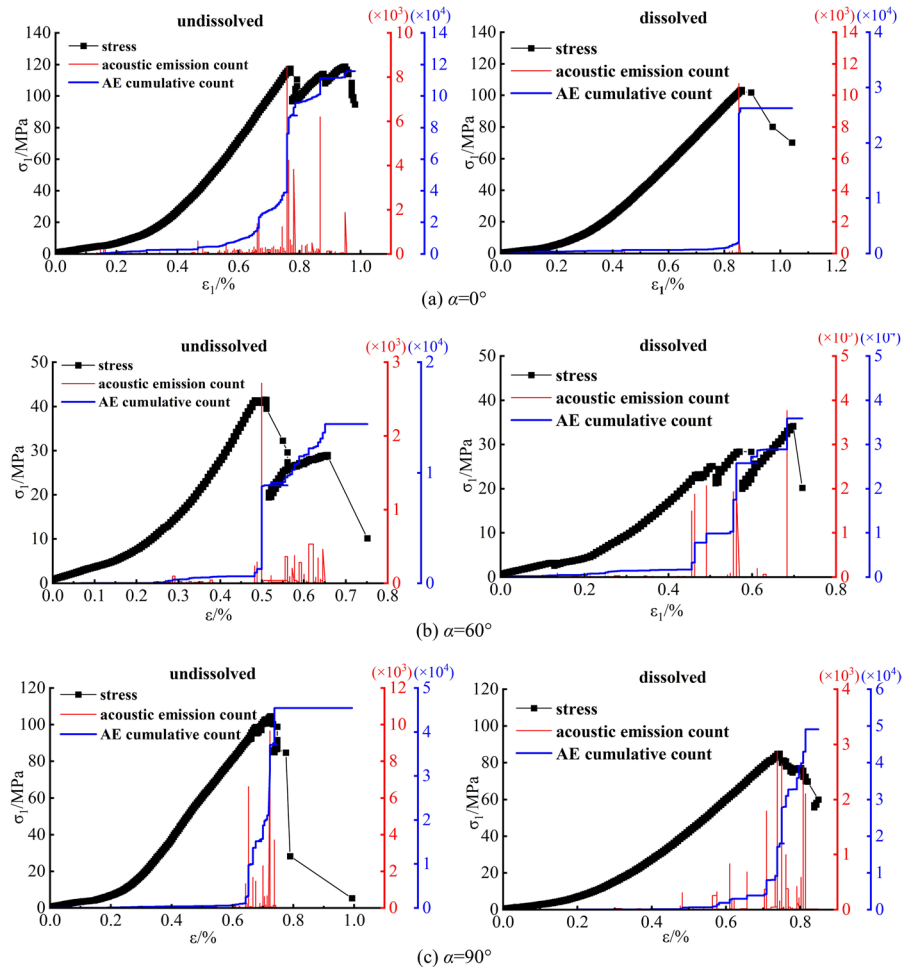
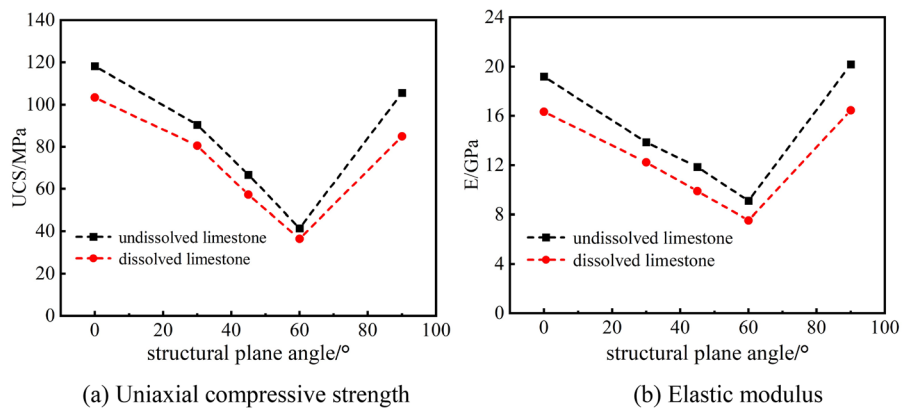


**Fig. 10** Uniaxial compressive strength and elastic modulus values of limestone samples with different bedding dip angles



the smallest when  $\alpha=60^\circ$ , near  $45^\circ + \varphi_f/2$  ( $\varphi_f$  is the internal friction angle of the structural plane) (Zhao 2019). The uniaxial compressive strength and elastic modulus values of the undissolved

limestone samples were greater than those of the dissolved limestone samples. Dissolution greatly damaged the limestone, and the mechanical properties were obviously reduced. At  $\alpha=0-90^\circ$ , the



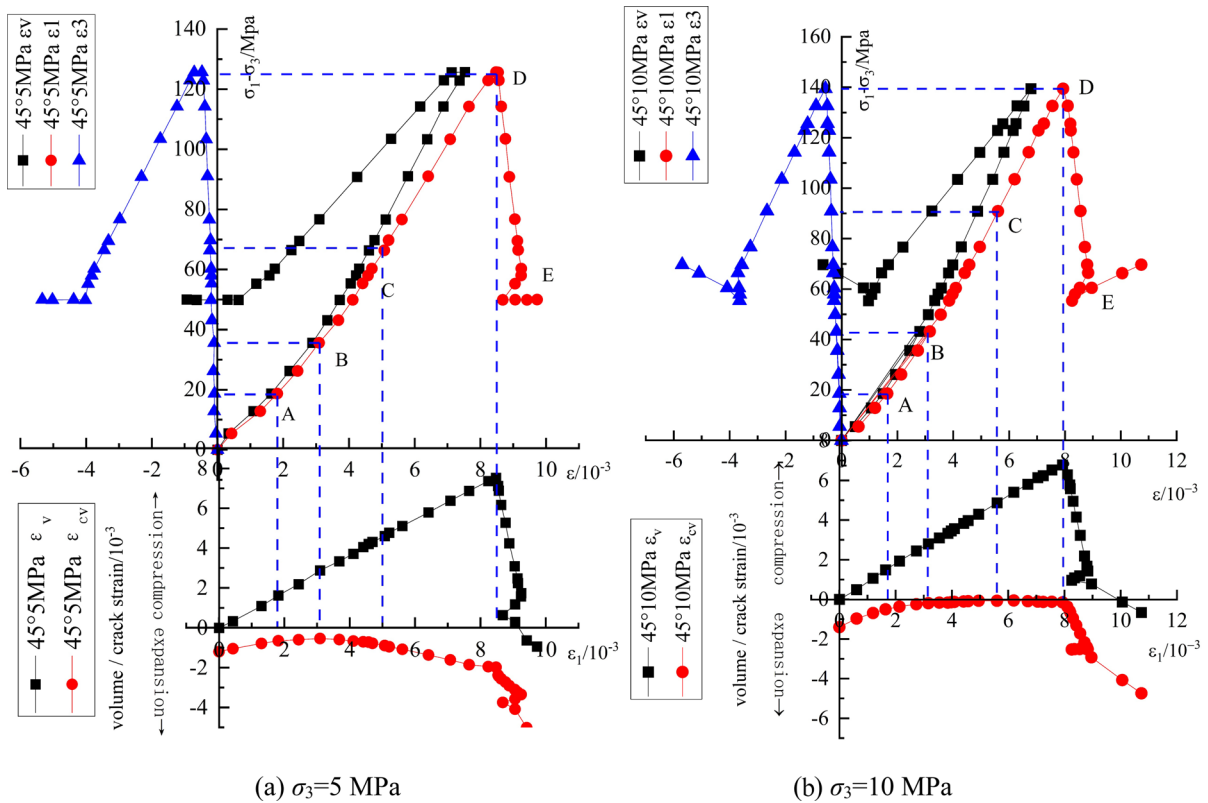


**Fig. 11** Stress–strain curves of the undissolved limestone samples ( $\alpha=45^\circ$ )

uniaxial compressive strengths of the dissolved limestone specimens decreased by 12.622, 10.974, 14.194, 12.145, and 19.693% compared with those of the corresponding undissolved limestone.

### 3.3.2 Results of the triaxial compression test

Martin (1997) proposed relationships among the volumetric strain, crack volumetric strain, and axial strain to determine the characteristic strengths of rocks. The volumetric strain ( $\epsilon_v$ ) was the total strain, which could be expressed by the elastic volumetric strain ( $\epsilon_{ev}$ ) and the crack volumetric strain ( $\epsilon_{cv}$ ). The elastic volumetric strain was related to the elastic modulus ( $E$ ) and Poisson’s ratio ( $\nu$ ). The calculation formulas for the elastic volumetric strain ( $\epsilon_{ev}$ ) and crack volumetric strain ( $\epsilon_{cv}$ ) were as follows (Wang et al. 2012, 2014; Zhang et al. 2022):

$$\epsilon_v = \epsilon_{ev} + \epsilon_{cv} \tag{1}$$

$$\epsilon_{ev} = \frac{1 - 2\nu}{E}(\sigma_1 + 2\sigma_3) \tag{2}$$

$$\epsilon_{cv} = \epsilon_v - \frac{1 - 2\nu}{E}(\sigma_1 + 2\sigma_3) \tag{3}$$

where  $\nu$  is Poisson’s ratio and  $\sigma_1$ ,  $\sigma_3$  and  $E$  are the axial stress, confining pressure, and elastic modulus (MPa), respectively.

According to the abovementioned method, the stress–strain curves of partially corroded samples and uncorroded samples under different confining pressures were drawn at bedding dip angles of  $45^\circ$  (Figs. 11 and 12).  $\sigma_1$ – $\sigma_3$  are the stresses,  $\epsilon_1$  is the axial strain,  $\epsilon_3$  is the circumferential strain,  $\epsilon_v$  is the volumetric strain ( $\epsilon_v = \Delta V/V_0 = \epsilon_1 + 2\epsilon_3$ ), and  $\epsilon_{ev}$  and  $\epsilon_{cv}$  are the elastic volumetric strain and crack volumetric strain, respectively. Compression is the positive direction of strain, and expansion is the negative direction of strain. In the figures, r-45°-5 MPa

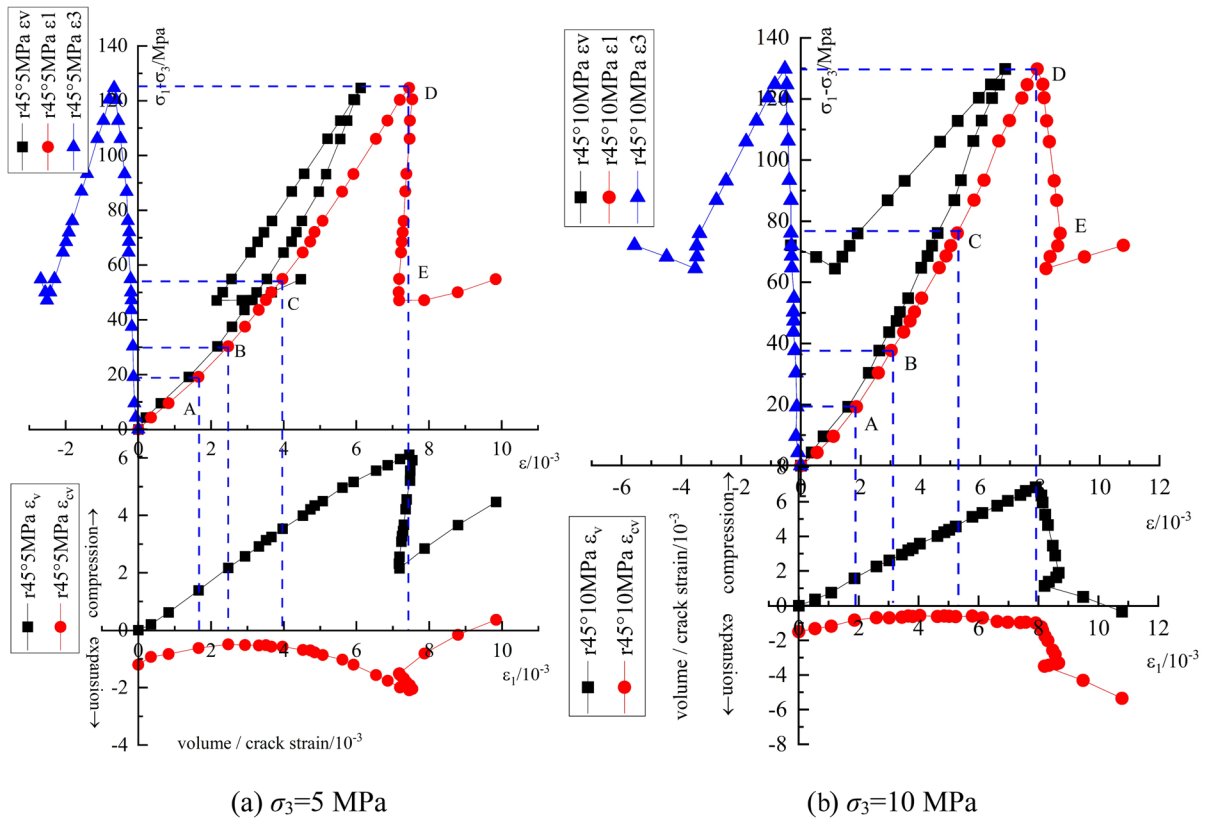


**Fig. 12** Stress–strain curves of the dissolved limestone samples ( $\alpha=45^\circ$ )

represents dissolution compression, with a bedding dip angle of  $45^\circ$  and a confining pressure of 5 MPa.

Figures 11 and 12 show that the total stress–strain curves could be divided into five stages during tri-axial loading. Stage I (OA) was the primary micro-fracture closure, and its upper stress was the fracture closure stress  $\sigma_{cc}$ . Stage II (AB) was the elastic compression stage, the upper stress value of which was the rock-initiating crack stress  $\sigma_{ci}$ . The crack volumetric strain peaked for compression and began to expand with crack growth. Stage III (BC) was the stage of stable crack development, and its upper stress value was the rock damage stress  $\sigma_{cd}$ . The volumetric strain peaked for compression, and the whole volume began to expand. Stage IV (CD) was the rapid crack development stage, and its upper stress value was the peak stress  $\sigma_c$ . Stage V (DE) was the stage of post-peak deformation and failure, and point E was the residual stress  $\sigma_{cr}$ . As the axial strain  $\epsilon_1$  increased, the variation trends of the relationship curves of  $(\sigma_1 - \sigma_3) - \epsilon_1$ ,  $(\sigma_1 - \sigma_3) - \epsilon_3$ ,  $(\sigma_1 - \sigma_3) - \epsilon_v$ ,  $\epsilon_v - \epsilon_1$ , and  $\epsilon_{cv} - \epsilon_1$

for the undissolved and dissolved limestone samples were similar under different bedding dip angles and confining pressures.

The characteristic stresses of the undissolved and dissolved limestone samples under the different test conditions are listed in Table 3. The corrosion effect reduced the mechanical strength of the rock mass in terms of crack initiation stress and damage stress. When the confining pressure was the same, the bedding dip angle controlled the crack growth, and the crack volume expansion rate at  $\alpha=45^\circ$  was faster than that at  $\alpha=0^\circ$ , which accelerated rock failure. The increasing confining stress decelerated rock failure. When  $\sigma_3=5$  MPa, the initiation crack stresses, damage stresses, and peak stresses of the dissolved limestone samples decreased by 23.79, 12.92, and 4.91%, respectively, at  $\alpha=0^\circ$  and by 14.89, 17.3, and 0.48%, respectively, at  $\alpha=45^\circ$  compared with those of the undissolved limestone. When  $\sigma_3=10$  MPa, the initiation crack stresses, damage stresses and peak stresses of the dissolved samples decreased by 14.99,

**Table 3** Strength characteristics of the rock masses under different loading conditions

Test condition	Initiation stress $\sigma_{ci}/\text{MPa}$	Damage stress $\sigma_{cd}/\text{MPa}$	Peak stress $\sigma_c/\text{MPa}$	Residual stress $\sigma_{cr}/\text{MPa}$
0° 5Mpa	63.6	151.36	198.09	55.63
0° 10Mpa	84.18	169.55	274.25	100.5
r0° 5Mpa	48.47	131.81	188.37	41.95
r0° 10Mpa	71.556	138.4	265.4	109.07
45° 5Mpa	35.64	66.4	126.1	50.64
45° 10Mpa	43.2	90.9	139.71	60.04
r45° 5Mpa	30.33	54.936	125.5	46.98
r45° 10Mpa	37.7	76.18	131.04	65.12

When the bedding angle is 0° and the confining pressure is 5 MPa, r0 is 5 MPa under the action of dissolution.

18.37, and 3.22%, respectively at  $\alpha=0^\circ$  and by 13.66, 16.19, and 6.21%, respectively, at  $\alpha=45^\circ$ .

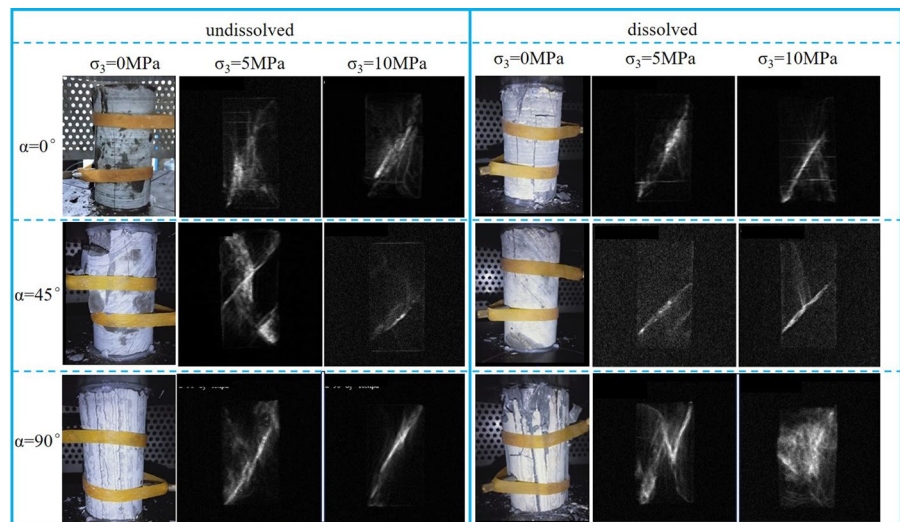
### 3.4 Failure mode

As shown in Fig. 13, when the confining pressure was 0 MPa, the failure modes of limestone with increasing bedding angle were mainly splitting failure, sliding failure along the bedding plane, and tensile failure along the bedding plane. When  $\alpha=0^\circ$ , the crack split and propagated along the axial direction, the horizontal layer stratified the vertical crack propagation, and the sample loosened and broke after failure. When  $\alpha=45^\circ$ , crack propagation was dominated by slip failure along the bedding plane, and some rotating cracks penetrated multiple bedding planes. The stress analysis showed that the tensile cracks broke

the matrix. When  $\alpha=90^\circ$ , the crack underwent tensile failure along the bedding plane. Through comparative analysis, there were differences in the compressive deformation and failure characteristics of limestone soaked in AMD solution. Dissolution led to the development of pores in the shallow surface of the limestone, and microcracks easily formed along the bedding planes and peeled off, which decreased the limestone strength.

As shown in Fig. 13. When  $\alpha=0^\circ$  and  $\sigma_3=5/10$  MPa, the failure mode of the undissolved sample was shear failure, the main crack expanded at oblique angles of approximately  $60^\circ \sim 70^\circ$ , and some branch cracks penetrated the matrix. When  $\alpha=0^\circ$  and  $\sigma_3=5$  MPa, the main crack of the dissolved sample was approximately  $60^\circ$ , and branch cracks were observed on the bedding plane. When

**Fig. 13** Typical failure diagrams of the triaxial compression tests and NMR imaging tests



$\sigma_3 = 10$  MPa, the main crack angle of the corrosion sample was approximately  $60^\circ$ , and a reverse crack with an angle of  $68^\circ$  formed simultaneously. The two main cracks formed the X-shaped crack, and the cracks propagated in many layers. When  $\alpha = 45^\circ$  and  $\sigma_3 = 5$  MPa under the control of the dip angle of the bedding plane, the main crack fracture angles of the undissolved and dissolved samples were all approximately  $45^\circ$ , and shear failure occurred along the bedding planes. When  $\sigma_3 = 10$  MPa, the mechanical strength of the limestone matrix decreased due to the influence of dissolution. Due to the inhibition of the confining pressure, branch cracks formed in the dissolution sample and propagated along the matrix. When  $\alpha = 90^\circ$  and  $\sigma_3 = 5$  MPa, the main crack of the undissolved sample was approximately  $57^\circ$ , and the limestone matrix was crushed. The corrosion samples showed Y-shaped cracks with angles of  $68^\circ$ . The local limestone matrix was crushed, and branch cracks formed. When  $\alpha = 90^\circ$  and  $\sigma_3 = 10$  MPa, a crack in the undissolved sample appeared at  $64^\circ$ , the limestone matrix was crushed to a reduced degree, and the main crack ran through the whole sample. The mechanical strength of the matrix of the dissolved sample decreased, and the whole matrix was crushed.

A difference was apparent in the triaxial compression failure mode between the dissolved and undissolved limestone specimens. When  $\alpha = 0^\circ$  or  $90^\circ$ , main cracks penetrating at shear angles of approximately  $60\text{--}70^\circ$  are formed, and after dissolution, additional branch cracks form in the limestone samples. When  $\alpha = 45^\circ$ , penetrating cracks obviously form along the bedding plane.

## 4 Chemical–mechanical damage model

### 4.1 Definition of the damage variable

Under the action of hydrochemical dissolution and external loading, a rock mass would be damaged, which would directly deteriorate its mechanical parameters and bearing capacity. According to the Lemaitre strain equivalence principle (Lemaitre 1984, 1985; Lemaitre et al. 1994), the strain caused by the nondestructive stress acting on the damaged material was equivalent to the strain caused by the effective

stress acting on the undamaged material. The expressions of chemical damage and mechanical damage were obtained by conversion (Jiang et al. 2011):

$$\varepsilon = \sigma / \tilde{E} = \tilde{\sigma} / E_0 = \sigma / E_0 (1 - D) \quad (4)$$

$$\begin{aligned} \sigma &= (1 - D)E_0\varepsilon = (1 - D_C)(1 - D_m)E_0\varepsilon \\ &= (1 - D_C - D_m + D_C D_m)E_0\varepsilon \end{aligned} \quad (5)$$

where  $\tilde{E}$  is the elastic modulus of the damaged materials,  $\tilde{\sigma}$  is the effective stress,  $D$  is the total damage variable,  $D_C$  is the damage value under chemical action,  $D_m$  is the damage variable in the compression process, and  $E_0$  and  $\varepsilon$  are the rock mechanical parameters in the initial state without damage.

#### 4.1.1 Chemical damage variable

The elastic modulus was used to analyze and measure the hydrochemical damage variable  $D_C$ :

$$D_C = 1 - \frac{E_C}{E_0} \quad (6)$$

where  $E_C$  is the elastic modulus of the limestone sample after hydrochemical dissolution.

According to the calculations, the chemical damage results are shown in Fig. 14. The analysis results revealed that the chemical damage characteristics of the limestone samples exhibited V-shaped distributions with increasing bedding angle under the same

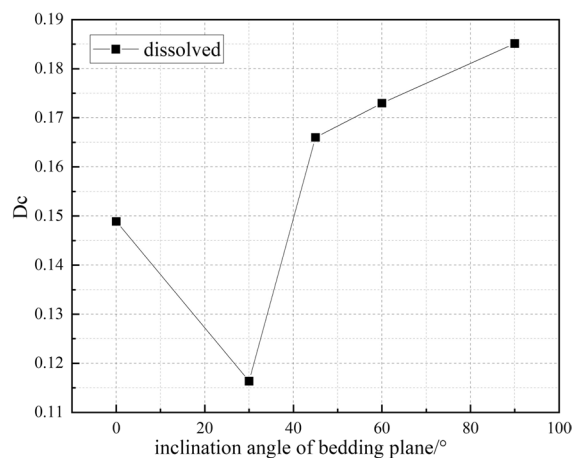


**Fig. 14** Chemical damage variables under dissolution conditions

dissolution conditions. The chemical damage values were between 0.10 and 0.20, indicating that AMD had obvious dissolution effects on the limestone samples. When  $\alpha > 30^\circ$ , the chemical damage to the limestone caused by dissolution was increasingly obvious. The bedding dip angle had a certain effect on controlling the chemical dissolution damage characteristics of the rock.

#### 4.1.2 Mechanical damage variable

In the field of rock mechanical damage calculations, many theories have been developed, including continuous damage theory, geometric damage theory, and fractal damage theory. Among these theories, research on continuous damage theory is the most mature and has been widely used (Wang 2017; Zhao 2019).

According to theoretical analysis, a rock mass could be divided into numerous microunits. Then, the ratio of the failure number of microelements  $N_f$  to the total number of microelements  $N$  could be used to define the cumulative effect of element failure (damage variable  $D_m$ ) during loading:

$$D_m = \frac{N_f}{N} \tag{7}$$

The Weibull distribution was suitable for describing the strength distributions of microunits (Shen et al. 2019). It was assumed that the limestone sample was composed of several microelements with different defects, and the microelement strength obeyed

the Weibull distribution function (Eq. 8) (Deng et al. 2011; Tang et al. 1990; Wong et al. 2006). The boundary conditions corresponding to the beginning and end of the test (Eq. 9) were substituted into Eq. (8) (Jiang et al. 2011; Zhang et al. 2019). The functional relationship between the mechanical damage variable and the strain was established by the integral derivative mathematical method (Eq. (10)).

$$\left. \begin{aligned} dD/dx &= \varphi(x) \\ \varphi(x) &= \frac{m}{\alpha} \left(\frac{x}{\alpha}\right)^{m-1} \exp\left[-\left(\frac{x}{\alpha}\right)^m\right] \end{aligned} \right\} \tag{8}$$

$$\left. \begin{aligned} \varepsilon = 0, \sigma = 0 \\ D = 0, d\sigma/d\varepsilon = E \\ \sigma = \sigma_f, \varepsilon = \varepsilon_f \\ \varepsilon = \varepsilon_f, d\sigma/d\varepsilon = 0 \end{aligned} \right\} \tag{9}$$

where  $\varphi(x)$  is the probability density function of the Weibull distribution;  $m$  is the shape factor of the distribution function, representing the uniformity of the rock;  $\alpha$  is the distribution factor, which represents the overall average value of the ultimate strain of the microelements;  $\sigma_f$  is the stress at the end of the test; and  $\varepsilon_f$  is the strain at the end of the test.

The variable was calculated as follows:

$$D_m = 1 - e^{-\left(\frac{\varepsilon}{\alpha}\right)^m} = 1 - e^{-\frac{1}{m} \left(\frac{\varepsilon}{\varepsilon_f}\right)^m} \tag{10}$$

The mechanical damage parameters of the undissolved and dissolved limestone samples with

**Table 4** Mechanical damage parameters of limestone specimens with different dip angles

Test condition		Undissolved				Dissolved			
Dip angle /°	Confining pressure / MPa	$\sigma_f$ /MPa	$\varepsilon_f$ %	E/GPa	m	$\sigma_f$ /MPa	$\varepsilon_f$ %	E/GPa	m
0	0	118.28	0.9492	19.174	2.32	103.35	0.8619	16.319	3.25
	5	198.09	1.28	18.508	5.58	188.37	1.25	15.753	22.55
	10	274.25	1.24	24.836	8.62	265	1.28	21.14	47.9
30	0	90.39	0.8080	13.846	4.69	80.47	0.9576	12.235	2.66
45	0	66.79	0.63	11.847	9.01	57.31	0.7599	9.88	3.7
	5	126.1	0.854	18.1471	4.8	125.5	0.75	18.2	9.96
	10	139.71	0.8	21.519	4.79	131.04	0.79	17.946	12.7
60	0	41.5	0.5104	9.1	8.88	36.46	0.7332	7.526	2.41
90	0	105.62	0.7268	20.179	3.05	84.82	0.6047	17.142	4.99

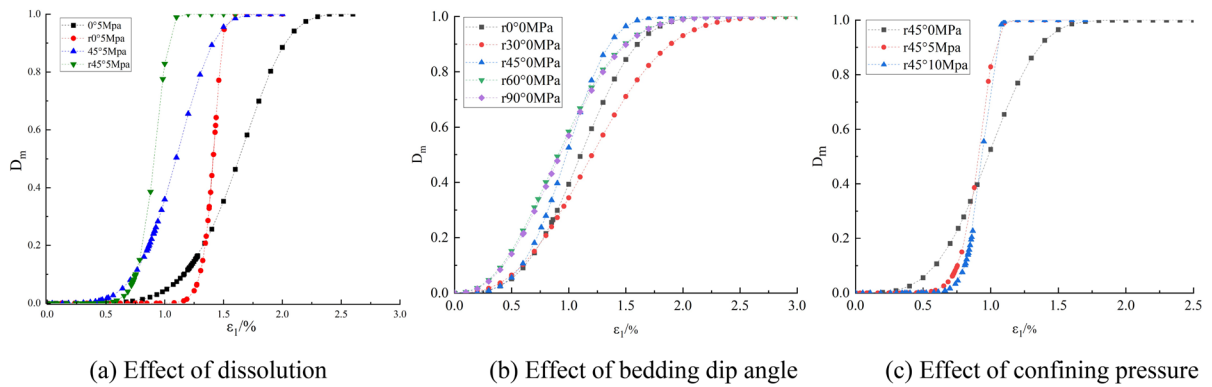


**Fig. 15** Evolution curves of the mechanical damage variables

different dip angles and confining pressures are listed in Table 4.

According to the calculation results in Fig. 15, the mechanical damage parameters of the undissolved and dissolved limestone specimens approached 0 at the initial stage of loading, and the microscopic voids of the rock were compacted and closed. When the stress exceeded its elastic limit, new microcracks and macrocracks continuously formed inside the sample, the circumferential strain increased, and the growth rate of the damage variable  $D_m$  gradually increased. When the fissures were interconnected, penetrating failure occurred, the strength of the sample sharply decreased, and the damage variable  $D_m$  approached 1.0. This phenomenon was consistent with the change in the acoustic emission signal during sample compression. The theoretical expression of the damage variable with respect to the strain was considered reasonable.

Figure 15a, b, and c show that dissolution, bedding dip angle, and confining pressure could influence the changes in the damage variable  $D_m$ . The damage to the dissolved limestone clearly increased during loading, and the damage variable  $D_m$  increased rapidly at a low strain level. When the damage variable  $D_m$  of a limestone sample with a bedding dip angle of  $45^\circ$  reached 1, the strain was the lowest, and the growth rate was the fastest. The  $D_m$  growth rates of the limestone samples with bedding dip angles of  $60^\circ$  and  $90^\circ$  were the second largest. With increasing confining pressure, in the

initial stage of loading, the internal damage of the sample was weak, and the damage growth accelerated in the later stages, with almost exponential growth.

#### 4.2 Modification of Damage to Stress–strain Curve

By substituting Eqs. (6–10) into Eq. (5), the specific functional expression of the mechanical parameter degradation was established.

$$\begin{aligned}\sigma &= (1 - D)E_0\varepsilon = (1 - D_C)(1 - D_m)E_0\varepsilon \\ &= (1 - D_C)E_0\varepsilon e^{-\frac{1}{m}\left(\frac{\varepsilon}{\varepsilon_f}\right)^m}\end{aligned}\quad (11)$$

The damage model in Eq. (11) could not reflect the characteristics of pore compaction under loading and had to be modified. During AMD-induced limestone corrosion, the number of pores increased. In the whole process of loading deformation, the initial compaction stage accounted for a large proportion, which could not be generally considered elastic deformation. Therefore, the compaction coefficient  $K$  was used to represent the deformation characteristics of the pore compaction stage. Based on previous studies (Liu et al. 2016, 2018; Xu et al. 2018), the compaction coefficient  $K$  was defined as the ratio of the slope of the stress–strain curve to the Young’s modulus  $E$  at the compaction stage, which could effectively describe the compaction characteristics of rock materials. However,

considering that in the compression and postfailure stages, the crack volumes of the samples underwent expansion instead of compression, and they basically presented logarithmic growth.  $K$  was adjusted as follows.

$$K = \begin{cases} \log_{n_1} \left( \frac{(n-1)\epsilon}{\epsilon_f} + 1 \right) & \epsilon \leq \epsilon_f \\ \log_{n_2} \left( \frac{\epsilon}{\epsilon_f} - 1 \right) & \epsilon > \epsilon_f \end{cases} \quad (12)$$

where  $n$ ,  $n_1$ , and  $n_2$  are experimental fitting constants.

In this work, the coefficient  $K$  was introduced, and the model was modified to the following expression:

$$\sigma = (1 - D)E_0\epsilon = (1 - D_C)(1 - D_m)E_0\epsilon = (1 - D_C)KE_0\epsilon e^{-\frac{1}{m} \left( \frac{\epsilon}{\epsilon_f} \right)^m} \quad (13)$$

Some of the bedding limestone compression data were selected for calculation via Eq. (13), and the modified stress–strain curve was obtained. As shown in Fig. 16, the modified mechanical model could effectively reflect the whole stress–strain curve characteristics of the bedding limestone and was highly consistent with the test curves.

### 5 Conclusions

(1) There were dissolution differences between the bedding planes and matrices of the limestone samples. During dissolution, the matrix crystals disappeared, and a serrated dissolution morphol-

ogy formed during calcite cleavage, which easily formed small pores. The dissolution of the bedding surface resulted in the formation of honeycomb-shaped dissolution pores, making it easy to produce large pores.

(2) With increasing bedding plane angle, the compressive strength and elastic modulus values of the limestone samples exhibited V-shaped distributions. Additional branch cracks were derived from the limestone samples after dissolution, and dissolution reduced the mechanical strength of the limestone from the aspects of crack initiation stress and damage stress. When the confining pressure was the same, the bedding angle affected the crack volume expansion.

(3) At  $\sigma_3=0$  MPa, with increasing bedding dip angle, the failure modes of the rock samples transitioned from matrix tensile failure and shear failure along the bedding plane to plane tensile failure. The triaxial compression failure modes between the dissolved and undissolved limestone specimens were different. When  $\alpha=0^\circ$  and  $90^\circ$ , additional branch cracks formed in the limestone sample after dissolution. When  $\alpha=45^\circ$ , the formation of controlled penetrating cracks along the bedding plane was increasingly obvious.

(4) By coupling the chemical damage variables and mechanical damage variables and by performing theoretical calculations, the stress–strain changes were predicted during the test.

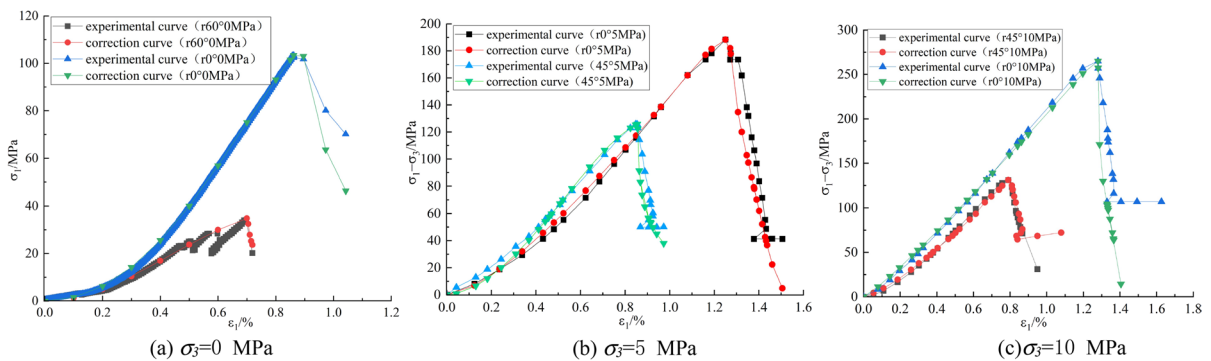


**Fig. 16** Comparison of the compression and modified curves of bedding limestone

A mechanical model considering chemical damage and mechanical damage was established and modified by the compaction coefficient  $K$ , which could effectively reflect the stress–strain process throughout rock sample compression.

This paper was only focused on microscopic morphological changes, mechanical properties, and one-dimensional damage constitutive models. This model for rocks under chemical–mechanical actions was verified. Further research on the three-dimensional damage constitutive model would be needed to provide a basis for theoretical research.

**Author contributions** All authors contributed to the study conception and design. Material preparation, data collection, and analysis were performed by Shuangying Zuo, Yunchuan Mo, and Chengyuan Ding. The first draft of the manuscript was written by Shuangying Zuo and Chengyuan Ding, and all authors commented on previous versions of the manuscript. All authors read and approved the final manuscript.

**Funding** This work is supported by the National Natural Science Foundation of China (Grant No. 42167025), and the Science and Technology Foundation of Guizhou Province ([2020]1Z052). They are gratefully acknowledged.

**Availability of data and materials** The data presented in this study are available on request from the corresponding author.

#### Declarations

**Ethics approval** Not applicable.

**Conflict of interests** No potential conflict of interest was reported by the author(s).

**Consent to publish** The authors declare that this paper has not been published previously and is not under consideration for publication elsewhere; its publication has been approved by all co-authors; its publication has been approved by the responsible authorities at the institution where the work is carried out; if accepted, it will not be published elsewhere in the same form. The authors agree to publication in “Geomechanics and Geophysics for Geo-Energy and Geo-Resources” and also to publication of the article in English by Springerature.

**Explanation** This work is the author’s related research results during the master’s study.

**Competing interests** There is no direct or indirect economic or non-economic conflict of interest in the works submitted to the publication.

**Open Access** This article is licensed under a Creative Commons Attribution 4.0 International License, which permits use, sharing, adaptation, distribution and reproduction in any medium or format, as long as you give appropriate credit to the original author(s) and the source, provide a link to the Creative Commons licence, and indicate if changes were made. The images or other third party material in this article are included in the article’s Creative Commons licence, unless indicated otherwise in a credit line to the material. If material is not included in the article’s Creative Commons licence and your intended use is not permitted by statutory regulation or exceeds the permitted use, you will need to obtain permission directly from the copyright holder. To view a copy of this licence, visit <http://creativecommons.org/licenses/by/4.0/>.

#### References

- Bai Y, Liu Q, Gu Z, Lu Y, Sheng Z (2019) The dissolution mechanism and karst development of carbonate rocks in karst rocky desertification area of Zhenfeng–Guanling–Huangjiang County, Guizhou, China. *Carbonates Evaporites* 34:45–51. <https://doi.org/10.1007/s13146-017-0386-x>
- Chen X, Liu X, Luo H, Long L, Liu C (2022) Microscopic damage to limestone under acidic conditions: phenomena and mechanisms. *Sustainability* 14:11771. <https://doi.org/10.3390/su141811771>
- Deng J, Gu D (2011) On a statistical damage constitutive model for rock materials. *Comput Geosci* 37:122–128. <https://doi.org/10.1016/j.cageo.2010.05.018>
- Fortes JC, Castilla-Gutierrez J, Sarmiento A, Grande JA (2022) Corrosion of carbon steel in extreme environments by acid mine water: experimental study of the process using a factorial analysis tool. *Minerals* 12:1030. <https://doi.org/10.3390/min12081030>
- Huang Z, Zeng W, Wu Y, Li S, Gu Q, Zhao K (2021) Effects of temperature and acid solution on the physical and tensile mechanical properties of red sandstones. *Environ Sci Pollut Res* 28:20608–20623. <https://doi.org/10.1007/s11356-020-11866-x>
- Huayan Y, Zhenhua Z (2016) Experimental study on influences of chemical solutions on mechanical properties of brittle limestone under triaxial compression. *Phys Numer Simul Geotech Eng* 23:79–85
- Jiang AN, Jiang SA (2012) Study on limestone uniaxial compression creep test with chemistry–mechanics coupling action. *Adv Mater Res* 378:453–456. <https://doi.org/10.4028/www.scientific.net/AMR.378-379.453>
- Jiang L, Wen Y (2011) Damage constitutive model of sandstone during corrosion by AMD. *J Cent South Univ (science and Technology)* 42:3502–3506
- Jiang C, Gao X, Hou B, Zhang S, Zhang J, Li C, Wang W (2020) Occurrence and environmental impact of coal mine goaf water in karst areas in China. *J Clean Prod* 275:123813. <https://doi.org/10.1016/j.jclepro.2020.123813>
- Lemaitre J (1984) How to use damage mechanics. *Nucl Eng Des* 80:233–245. [https://doi.org/10.1016/0029-5493\(84\)90169-9](https://doi.org/10.1016/0029-5493(84)90169-9)



- Lemaitre J (1985) A continuous damage mechanics model for ductile fracture <https://doi.org/10.1115/1.3225775>
- Lemaitre J, Chaboche J-L (1994) *Mechanics of solid materials*. Cambridge University Press, Cambridge
- Li H, Yang D, Zhong Z, Sheng Y, Liu X (2018a) Experimental investigation on the micro damage evolution of chemical corroded limestone subjected to cyclic loads. *Int J Fatigue* 113:23–32. <https://doi.org/10.1016/j.ijfatigue.2018.03.022>
- Li H, Zhong Z, Liu X, Sheng Y, Yang D (2018b) Micro-damage evolution and macro-mechanical property degradation of limestone due to chemical effects. *Int J Rock Mech Min Sci* 110:257–265. <https://doi.org/10.1016/j.ijrmmms.2018.07.011>
- Li H, Zhong Z, Eshiet KI-I, Sheng Y, Liu X, Yang D (2020) Experimental investigation of the permeability and mechanical behaviours of chemically corroded limestone under different unloading conditions. *Rock Mech Rock Eng* 53:1587–1603. <https://doi.org/10.1007/s00603-019-01961-y>
- Liu X, Ning J, Tan Y, Gu Q (2016) Damage constitutive model based on energy dissipation for intact rock subjected to cyclic loading. *Int J Rock Mech Min Sci* 85:27–32. <https://doi.org/10.1016/j.ijrmmms.2016.03.003>
- Liu X, Tan Y, Ning J, Lu Y, Gu Q (2018) Mechanical properties and damage constitutive model of coal in coal-rock combined body. *Int J Rock Mech Min Sci* 110:140–150. <https://doi.org/10.1016/j.ijrmmms.2018.07.020>
- Liu X, Deng W, Wang S, Liu B, Liu Q (2023a) Experimental investigation on microstructure and surface morphology deterioration of limestone exposed on acidic environment. *Constr Build Mater* 377:131065. <https://doi.org/10.1016/j.conbuildmat.2023.131065>
- Liu X, Wang S, Liu B, Chen J, Liu Q, Luo J (2023b) Effect of microstructure on changes to the pore structure and mechanical properties of limestone under acidic groundwater corrosion. *Int J Geomech* 23:04023212. <https://doi.org/10.1061/JGNALGMENG-8847>
- Martin CD (1997) Seventeenth Canadian geotechnical colloquium: the effect of cohesion loss and stress path on brittle rock strength. *Can Geotech J* 34:698–725. <https://doi.org/10.1139/t97-030>
- Retka J, Rzepa G, Bajda T, DREWNIAK L (2020) The use of mining waste materials for the treatment of acid and alkaline mine wastewater. *Minerals* 10:1061. <https://doi.org/10.3390/min10121061>
- Rodríguez C, Leiva-Aravena E, Serrano J, Leiva E (2018) Occurrence and removal of copper and aluminum in a stream confluence affected by acid mine drainage. *Water* 10:516. <https://doi.org/10.3390/w10040516>
- Santos Jallath JE, Romero FM, Iturbe Argüelles R, Cervantes Macedo A, Goslinga Arenas J (2018) Acid drainage neutralization and trace metals removal by a two-step system with carbonated rocks, Estado de Mexico, Mexico. *Environ Earth Sci* 77:1–18. <https://doi.org/10.1007/s12665-018-7248-2>
- Shen P, Tang H, Ning Y, Xia D (2019) A damage mechanics based on the constitutive model for strain-softening rocks. *Eng Fract Mech* 216:106521. <https://doi.org/10.1016/j.engfractmech.2019.106521>
- Tang C, Xu X (1990) Evolution and propagation of material defects and Kaiser effect function. *J Seismol Res* 13:203–213
- Wang B, Zhu J, Yan P, Huang S, Wu A (2012) Damage strength determination of marble and its parameters evaluation based on damage control test. *Chin J Rock Mech Eng* 31:3967–3973
- Wang S (2017) The effect and numerical analysis on mechanical parameters of surrounding rock in the process of tunnel excavation unloading damage. Dissertation, Guizhou University
- Wang Y, Li X, Wu Y, Ben Y, Li D, He J, Zhang B (2014) Research on relationship between crack initiation stress level and brittle indices for brittle rocks. *Chin J Rock Mech Eng* 33:264–275. <https://doi.org/10.13722/j.cnki.jrme.2014.02.003>
- Wong T-f, Wong RH, Chau KT, Tang C (2006) Microcrack statistics, Weibull distribution and micromechanical modeling of compressive failure in rock. *Mech Mater* 38:664–681. <https://doi.org/10.1016/j.mechmat.2005.12.002>
- Xia S, Song Z, Zhao X, Li J (2023) Review of the recent advances in the prevention, treatment, and resource recovery of acid mine wastewater discharged in coal mines. *J Water Process Eng* 52:103555. <https://doi.org/10.1016/j.jwpe.2023.103555>
- Xu X, Gao F, Zhang Z (2018) Thermo-mechanical coupling damage constitutive model of rock based on the Hoek-Brown strength criterion. *Int J Damage Mech* 27:1213–1230. <https://doi.org/10.1177/1056789517726838>
- Xu P, Sheng M, Lin T, Liu Q, Wang X, Khan WA, Xu Q (2022a) Influences of rock microstructure on acid dissolution at a dolomite surface. *Geothermics* 100:102324. <https://doi.org/10.1016/j.geothermics.2021.102324>
- Xu Q, Tian A, Luo X, Liao X, Tang Q (2022b) Chemical damage constitutive model establishment and the energy analysis of rocks under water-rock interaction. *Energies* 15:9386. <https://doi.org/10.3390/en15249386>
- Yu Y, Wang J, Feng G-L, Geng D-X, Guo H-S (2023) Damage evolution and acoustic emission characteristics of hydrochemically corroded limestone. *Bull Eng Geol Env* 82:112. <https://doi.org/10.1007/s10064-023-03128-0>
- Yuan L, Jiang Y, Wang K, Zhao Y, Hao X, Xu C (2018) Precision exploitation and utilization of closed/abandoned mine resources in China. *J China Coal Soc* 43:14–20. <https://doi.org/10.13225/j.cnki.jccs.2017.1803>
- Zhang Y, Zuo S, Yu B, Chen S, Jia J (2019) Study on bending damage constitutive model and mechanical properties of limestone based on acoustic emission. *Adv Civil Eng* 2019:1–10. <https://doi.org/10.1155/2019/2031520>
- Zhang H, Zhong Y, Zhang J, Zhang Y, Kuang J, Yang B (2020) Experimental research on deterioration of mechanical properties of carbonate rocks under acidified conditions. *J Petrol Sci Eng* 185:106612. <https://doi.org/10.1016/j.petrol.2019.106612>
- Zhang Y, Wang Z, Su G, Wu Z, Liu F (2022) Experimental investigation on influence of acidic dry-wet cycles on karst limestone deterioration and damage. *Geofluids*. <https://doi.org/10.1155/2022/8562226>
- Zhao D (2019) Stability analysis of tunnel surrounding rock based on transverse isotropic damage model. Dissertation, Guizhou University
- Zhu M, Li B, Liu G (2022) Groundwater risk assessment of abandoned mines based on pressure-state-response—The example of an abandoned mine in southwest China. *Energy Rep* 8:10728–10740. <https://doi.org/10.1016/j.egy.2022.08.171>

**Publisher's Note** Springer Nature remains neutral with regard to jurisdictional claims in published maps and institutional affiliations.